Generative Adversarial Models for Extreme Downscaling of Climate Datasets

Guiye Li and Guofeng Cao

Abstract—Addressing the challenges of climate change requires accurate and high-resolution mapping of climate and weather variables. However, many existing climate datasets, such as the gridded outputs of the state-of-the-art numerical climate models (e.g., general circulation models), are only available at very coarse spatial resolutions due to the model complexity and extremely high computational demand. Deep-learning-based methods, particularly generative adversarial networks (GANs) and their variants, have proved effective for refining natural images, and have shown great promise in improving scientific datasets. In this paper, we describe a conditional GAN-based geospatial downscaling method for extreme downscaling of gridded climate datasets. Compared to most existing methods, the method can generate high-resolution accurate climate datasets from very low-resolution inputs. More importantly, the method explicitly considers the uncertainty inherent to the downscaling process that tends to be ignored in existing methods. Given an input, the method can produce a multitude of plausible high-resolution samples instead of one single deterministic result. These samples allow for an empirical exploration and inferences of model uncertainty and robustness. With a case study of gridded climate datasets (wind velocity and solar irradiance), we demonstrate the performances of the framework in downscaling tasks with very high scaling factors (up to $64\times$) and highlight the advantages of the framework with a comprehensive comparison with commonly used downscaling methods, including area-to-point (ATP) kriging, deep image prior (DIP), enhanced deep super-resolution network (EDSR), enhanced super-resolution generative adversarial networks (ESRGAN), and physics-informed resolution-enhancing GAN (PhIRE GAN).

Index Terms—Stochastic downscaling, uncertainty modeling, deep learning, generative models, climate modeling

I. INTRODUCTION

CURATE and high-resolution mappings of climate variables are crucial for climate-related research and decision-making. Many climate models, such as general circulation models, are numerical models that mathematically describe the intricate, non-linear dynamics of the climate system and the complex interplay between climate factors [1]. Due to the inherent complexity, these numerical models are often extremely demanding for computational resources. Even with high-performance computers, they can only operate on grids with relatively coarse spatial resolutions. Consequently, the outputs of the numerical models often fall short in capturing the important details of spatial variations in climate variables. It highlights the need for effective downscaling methods to

Corresponding author: Guofeng Cao.

Guiye Li and Guofeng Cao are with the Department of Geography, University of Colorado Boulder, Boulder, CO, 80309-0260, USA. (e-mail: Guiye.Li@colorado.edu; Guofeng.Cao@colorado.edu)

improve gridded climate datasets and other gridded scientific datasets in general [2], [3].

The concept of downscaling is to make estimations at a finer spatial scale than that of the original datasets, aiming to enhance information and details. Within climate sciences, many climate downscaling methods have been developed and generally fall into two categories: process-based models and statistical downscaling methods [4], [5]. Process-based models focus on the numerical modeling of regional or nested climate dynamics, which can also be computationally demanding. The statistical methods, on the other hand, aim to enhance the spatial details by modeling spatial patterns and leveraging the empirical relations between coarse and fine-scale climate variables. Statistical downscaling is a traditional task shared by many related disciplines. Scale is inherent to spatiotemporal data and changing spatiotemporal scales is one of the most fundamental problems in GIScience and spatial statistics [6], [7]. In computer vision and machine learning, a closely related topic is image super-resolution (SR), which is to reconstruct high-resolution (HR) images from low-resolution (LR) images. In recent years, with the advancements of deep neural networkbased methods [8], a multitude of image SR methods have emerged to harness the power of deep neural network structures in representing intricate spatial patterns. The deep neural network structures, particularly convolutional neural networks (CNNs), equipped with a substantial amount of learnable weights, can effectively model and capture the complex spatial patterns embedded in LR images, and generate HR images that exhibit the minimal discrepancy when compared to LR images. These deep learning-based SR methods have shown superior performance compared to traditional methods in image SR; see [9]–[11] for reviews of the recent advancements.

The deep learning-based SR methods have been successfully applied for downscaling climate and scientific datasets [12]-[14]. Despite the success, climate and scientific measurements are inherently different from natural images that the most SR methods were developed for, and hence poses additional challenges for downscaling methods. First, uncertainty is an unavoidable property of scientific measurements [15], [16], and it is vital to characterize the uncertainty and understand the impact in scientific models and decision-making [17]. Downscaling is a typical inverse problem [18] that does not have a unique solution; a number of HR images can correspond to the exact same LR image, and the number of images grows exponentially as scaling factor increases. Thus downscaling process inevitably introduce new uncertainty to the results, and successful downscaling methods should capture the one-tomany mappings between LR and HR images. While significant

advancements have been made in uncertainty quantification in deep learning methods [19]-[23], most of the deep learningbased downscaling methods tend to produce deterministic results, often overlooking such uncertainty. Secondly, scientific datasets often exhibits a wide varieties of spatial resolutions, ranging from tens of kilometers to mere meters. Harmonizing this broad spectrum of spatial resolution requires downscaling methods can function effectively with high scaling factors. We refer the downscaling tasks with very high scaling factors (e.g., $64\times$) as extreme downscaling. In this study, we aim to address theses challenges by taking advantages of the advancements in generative adversarial networks. Furthermore, the pixel values of scientific datasets bear physical meanings of geographic regions. In the absences of additional information, downscaled results should be aligned with the original inputs. It is known as mass-preserving or pycnophylactic property in GIScience and geostatistics literature [24]–[27].

Within the spectrum of deep learning architectures, generative adversarial networks (GANs) [28] and the variant conditional GAN (CGAN) [29], provide a particularly powerful framework for stochastic image SR and other image restoration tasks [30]-[32]. A GAN includes two integral components, generator and discriminator (or critic), both commonly realized through neural networks. When conditional data such as LR images v are available, the *generator* can be described as a function $G_{\theta}(\mathbf{z}, \mathbf{y})$ regulated by learnable parameters θ , where z is a random vector with a known probability distribution (e.g., a Gaussian distribution). The main goal of the generator is to model the high-dimensional posterior distribution of HR images x guided by y, $\mathbb{P}_{x|y}$ with the help of z, or convert z to $\mathbf{g}_{\theta} = G_{\theta}(\mathbf{z}, \mathbf{y})$ such that $\mathbf{g}_{\theta} \mid \mathbf{y} \sim \mathbb{P}_{\mathbf{x} \mid \mathbf{y}}$. In contrast, the critic function, $C_{\omega}(\mathbf{x}, \mathbf{y})$ regulated by learnable parameters ω , acts as an adversary to the generator with a goal of discriminating $G_{\theta}(\mathbf{z}, \mathbf{y})$ from $\mathbb{P}_{\mathbf{x}|\mathbf{y}}$. The generator $G(\mathbf{z}, \mathbf{y})$ and critic $C(\mathbf{x}, \mathbf{y})$ operate in a adversary manner, undergoing simultaneous training through a two-player minimax game framework. Training a CGAN amounts to modeling the high-dimensional posterior distribution of HR images given LR images through a deep learning approach. The GAN-based models are free of the assumptions in traditional theory of statistics and probability, flexible in capturing complex spatial patterns, and yet share the generative properties of probability distributions. These properties render CGAN a suitable framework for uncertaintyaware scientific downscaling.

Recent work has emerged to take advantages of the CGAN in stochastic climate downscaling. Notable examples include [14], [33], [34], which used the CGANs to downscale the gridded scientific datasets and to explore the uncertainty of outcomes with generated samples. However, these CGANs often operate under the assumption that pairs of LR and HR are deterministic, thereby failing to capture the one-to-many stochasticity discussed previously and possibly leading to mode collapse [35]. Moreover, these CGANs were not designed for downscaling with high scaling factors. Progresses were made recently in addressing these issues. Particularly, a variant of CGAN, namely latent adversarial generator (LAG) [36], was proposed to account for the stochasticity of one-to-many mappings in the downscaling process by assuming a HR

image is a possibility rather than a single choice corresponding to LR images. This is achieved by learning a Gaussian distributed latent variable representing the distances between prediction and ground truth. To support super-resolution with high scaling factors, a progressive training strategy for GAN (ProGAN [37]) was developed. Starting with a low image scaling factor, the model captures incrementally fine details by adding new layers as the training progresses and the factor increases. This strategy has been proven to not only expedite the training process and enhance stability but also to better capture variations across multiple scales [37].

In this study, we describe a stochastic downscaling framework for extreme downscaling of gridded scientific datasets, leveraging both LAG [36] and ProGAN [37]. The framework enjoys the advantages of both sides and can efficiently address the previously discussed challenges in scientific downscaling: LAG for uncertainty and ProGAN for high scaling factors. With case studies of gridded climate datasets (wind velocity and solar irradiance), we demonstrate the performances of the framework in downscaling tasks with high scaling factors (e.g., $64\times$) and highlight the advantages of the framework with a comprehensive comparison with commonly used downscaling methods, including area-to-point (ATP) kriging [25], deep image prior (DIP) [38], enhanced deep super-resolution network (EDSR) [39], enhanced super-resolution generative adversarial networks (ESRGAN) [31], and physics-informed resolutionenhancing GAN (PhIRE GAN) [13]. The mass-preservation and the uncertainty space of the trained LAG-based models are also examined.

The contributions of this work are summarized as follows:

- 1) We describe a LAG-based downscaling framework for extreme downscaling of gridded scientific datasets that can account for complex spatial patterns and uncertainty;
- We demonstrate the performances of the framework with a high scaling factor (up to 64× for the wind velocity and solar irradiance data) and conduct a comprehensive performance comparison with commonly used downscaling methods;
- We examine the uncertainty and robustness of the LAGbased models with a simulation-based approach and check the mass-preservation of the model outputs.

The rest of this article is organized as follows: Section II introduces background and related work to this study. Section III presents the details of the described LAG-based downscaling framework. Section IV provides the experimental results of the framework applied to gridded climate datasets, and highlights the advantages of the LAG-based framework. Section VI concludes this paper and discusses future work.

II. RELATED WORK

A. Geostatistical methods

Downscaling images or gridded datasets can be taken as a particular case of the traditional change of spatial support problem (COSP) in spatial statistics [40], [41] or modifiable areal unit problem in GIScience [25], [41]–[43]. Numerous frameworks have been established within statistics and GI-Science to address these problems, many of which have been

applied for image downscaling. For example, in geostatistics the area-to-point kriging (ATPK) [25], [26], was developed to make predictions at points from areal aggregations, and has been widely adopted for downscaling satellite images [44]–[47] and gridded scientific data [48].

Kriging methods enjoy many advantages. Grounded in statistics theory, they provide measures of reliability or uncertainty for predictions [25], [26]. They can yield coherent and mass-preserving predictions that are important for scientific modeling. It means the statistics of disaggregated pixels (e.g., average) in downscaled images are aligned with the values of the associated coarse pixels in the original images. Furthermore, kriging methods provide effective tools, such as variograms, to examine the spatial patterns inherent in spatial datasets. Despite the advantages, as in other traditional statistical methods, kriging methods were developed under statistical assumptions that can be difficult to satisfy in practice. The reliance on two-point statistics such as covariance functions limits the performances in modeling complex spatial patterns [49].

B. Deep learning methods

1) GAN-based methods: As mentioned previously, the GAN-based models, CGANs in particular, have demonstrated successes in image super-resolution and shown potential in addressing the challenges in climate downscaling. Unlike GANs, CGANs feed the generator with additional data, such as an LR image, to guide the generation of HR outcomes. See [50] for a recent review of the such methods. Among these methods, super-resolution GAN (SRGAN) [30], Enhanced Deep Super-Resolution (EDSR) [39] and Enhanced Super-Resolution GAN (ESRGAN) [31] are perhaps most commonly used [51], [52]. SRGAN integrated a ResNet-based deep neural network architecture (SRResNet) into the GAN framework. SRGAN designed a perceptual loss function to ensure the high perceptual quality and peak signal-to-noise ratios of the outcomes. The perceptual loss consists of an adversarial loss and a content loss based on VGG models [53]: the former encourages the output align with the manifold of training images while the latter maintains the perceptual similarity with input images. Based on SRGAN, EDSR is a lightweight and efficient SR network that removes the batch normalization layer and ending activation layer in the residual block of the original SRResNet for simplicity and better performance [39]. ESRGAN enhance the SRGAN in network structure and loss functions to further reduce the artifacts of the generated images [31]. These GAN-based methods have been widely applied for downscaling scientific datasets including remote sensing imagery, and meteorological measurements [13], [33], [51].

2) Stochastic downscaling with GAN: Most of the aforementioned CGAN-based methods were designed for a single deterministic HR output. Notable progresses were made to introduce stochasticity to these CGAN-based methods to allow generating a set of plausible HR images for a given LR image [33], [54]. The stochasticity is important to assess the uncertainty and reliability associated with model output. Several methods were developed to allow stochasticity in

image SR. For instances, PULSE explores the latent spaces of the pre-trained GANs and samples the possible HR images that are downscalable from given LR images [55]. In unsupervised learning, deep image prior (DIP) [38] showed the neural network structure can serve as an image prior that can be stochastically sampled from and achieved the comparable performances with supervised methods. Many of these methods, however, treated the (x, y) pair as deterministic, and attempted to estimate the posterior distribution $\mathbb{P}_{\mathbf{x}|\mathbf{y}}$ using only a single sample x for each y. Consequently, these approaches may result in mode collapse [35], [56] and are unable to effectively consider the inherent uncertainty arising from the one-to-many mappings involved in the downscaling process. In contrast, LAG was recently proposed to assume a HR image is one sample from the manifold of LR images and introduced a Gaussian-like latent space to quantify the distances between LR and HR images [36].

3) Extreme climate downscaling: Applying GAN-based methods for downscaling tasks with very high scaling factors (e.g., 64×) can lead to unstable training process and mode collapses [57], [58]. When mode collapse happens, the generator produces similar or a limited variety of outputs. One effective strategy to mitigate this is to break down the training process into multiple steps. For instance, PhIRE GAN adopts deep CNNs and SRGAN for a two-step SR [13]. The SR model in the first step produces images from LR to medium resolution (MR), and the SR model in the second step is responsible for MR to HR. With the two-step process, the PhIRE GAN achieved up to 50× resolution enhancement for the Global Climate Model (GCM) outputs while preserving physically relevant characteristics. To streamline the process, ProGAN was recently developed to train the GAN models progressively, which facilitate the extreme downscaling [37].

III. METHODOLOGY

Given a LR image y, our goal is to sample from $\mathbb{P}_{\mathbf{x}|\mathbf{y}}$, the high-dimensional posterior distribution of HR images x that are possible downscaling outcomes of y. With the help of a random vector z, CGAN achieved this by mapping a pair of (\mathbf{z}, \mathbf{y}) to $\mathbf{g}_{\theta} = G_{\theta}(\mathbf{z}, \mathbf{y})$ such that $\mathbf{g}_{\theta} \mid \mathbf{y} \sim \mathbb{P}_{\mathbf{x} \mid \mathbf{y}}$. Hence, sampling from z effectively corresponds to sampling from $\mathbb{P}_{\mathbf{x}|\mathbf{y}}$. To avoid mode collapse and to account for the stochasticity in the one-to-many mappings in the downscaling process discussed previously, we adopt a method inspired by LAG [36]. As in other CGAN methods, LAG employs a simple Gaussian random vector $\mathbf{z} \in \mathbb{R}^N, \mathbf{z} \sim \mathcal{N}(\mathbf{0}, \mathbf{1})$. Within a CGAN framework, it further assumes that possible HR images x corresponding to a LR image y follows a latent Gaussianlike distribution centered around LR images $\mathcal{P}_{\mathbf{z},\mathbf{v}}(\mathbf{x})$, and that the most possible HR image should occur in the distribution center when z = 0. The assumption explicitly considers the stochastic links between x and y, and can be implemented by introducing an additional regularization term in the generator loss, which will be detailed in the following of this section.

A. Loss functions

To accurately model the posterior distribution $\mathbb{P}_{\mathbf{x}|\mathbf{y}}$ with the generator $G_{\theta}(\mathbf{x}, \mathbf{y})$, it is important to seek optimal generator

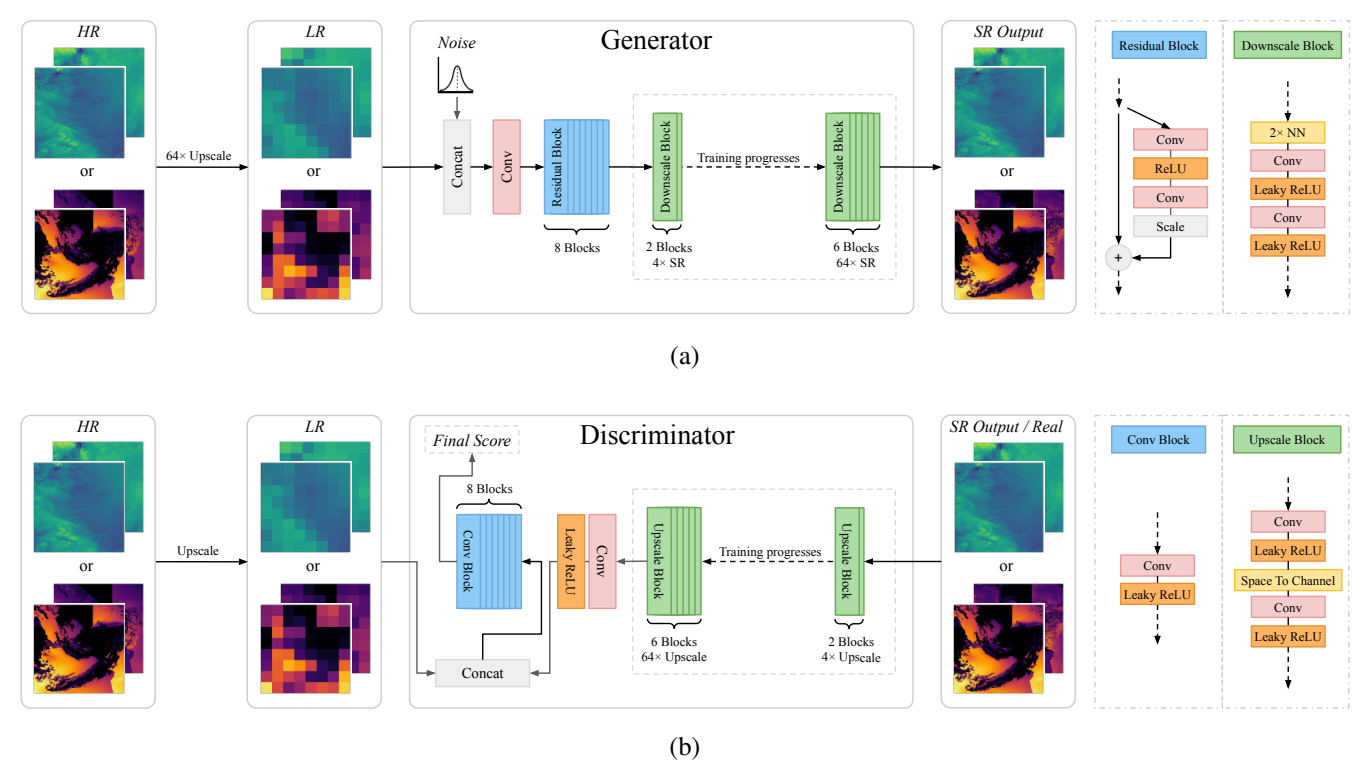


Fig. 1. Structures of the generator and discriminator in the described LAG-based downscaling framework: (a) Generator; (b) Discriminator.

and critic parameters that can minimize the discrepancy between $\mathbb{P}_{\mathbf{x}|\mathbf{y}}$ and $\mathbb{P}_{\mathbf{g}_{\boldsymbol{\theta}}|\mathbf{y}}$. In GAN literature, different types of loss functions were defined to quantify the discrepancy while keeping the balance between perceptual quality and distortion [59]. As in LAG, we adopt the Wasserstein GAN (WGAN) loss with gradient penalty [60], [61] in this study. To capture the proposed stochastic relationship between \mathbf{x} and \mathbf{y} , an additional regularization term was introduced to the WGAN loss function:

$$\mathcal{L}(\mathbb{P}_{\mathbf{x}|\mathbf{y}}, \mathbb{P}_{\mathbf{g}_{\boldsymbol{\theta}}|\mathbf{y}}|\boldsymbol{\theta}, \boldsymbol{\omega}) = \mathcal{L}_{wgan}(\mathbf{x}, \mathbf{y}) + \lambda_{gp} \cdot \mathcal{L}_{gp}(\mathbf{x}, \mathbf{y}) + \lambda \cdot \mathcal{L}_{center}(\mathbf{x}, \mathbf{y})$$
(1)

where $\mathcal{L}_{wgan}(\cdot,\cdot)$ indicates the regular WGAN loss [60], $\mathcal{L}_{gp}(\cdot,\cdot)$ is the gradient penalty to enforce the 1-Lipschitz constraints on critic function [61], λ_{gp} and λ are the regularization coefficients. The term $\mathcal{L}_{center}(\cdot,\cdot)$ is the introduced regularization term penalizing deviations of \mathbf{x} from the center of the latent distribution \mathcal{P} , which can be written as:

$$\mathcal{L}_{center}(\mathbf{x}, \mathbf{y}) = \mathbb{E}_{\mathbf{x}, \mathbf{y}}[||P(\mathbf{x}, \mathbf{y}) - P(G_{\theta}(\mathbf{0}|\mathbf{y}), \mathbf{y})||_{2}^{2}]$$
 (2)

The function $P(\mathbf{x}, \mathbf{y})$, as defined in Eq. 2, maps \mathbf{x} into a location on the latent distribution \mathcal{P} . This function, implemented in a deep neural network architecture, is designed to capture the complex spatial patterns in \mathbf{x} . The notation $G_{\theta}(\mathbf{0}, \mathbf{y})$ represents the center of the latent distribution. The logic of the loss function $\mathcal{L}_{center}(\mathbf{x}, \mathbf{y})$ is the ground truth (in the training process) or the most likely image (in the sampling process) should be close to the distribution center. This allows for a HR image \mathbf{x} to be taken as just one possible

outcome of downscaled \mathbf{y} , instead of a single, deterministic result. In doing so, it accounts for the intrinsic variability in the downscaling process and contributes to the mitigation of mode collapse by allowing multiple potential downscaling solutions. From $P(\mathbf{x}, \mathbf{y})$, the ciritic function can be derived, i.e., $C_{\boldsymbol{\omega}}(\mathbf{x}, \mathbf{y}) = F(P(\mathbf{x}, \mathbf{y}))$, where $F(\cdot)$ maps the locations in \mathcal{P} into a scalar critic score. For the mapping function $F(\cdot)$, simple mathematical operators are applicable. In this study, the mean operator is employed.

To summarize, the loss function in Eq. 1 can be expanded into Eq. 3, and as in CGAN, the generator G_{θ} and critic C_{ω} are trained via a two-player minimax game:

$$\min_{\boldsymbol{\theta}} \max_{\boldsymbol{\omega}} \mathbb{E}_{\mathbf{x}}[C_{\boldsymbol{\omega}}(\mathbf{x}, \mathbf{y})] - \mathbb{E}_{\mathbf{z}}[C_{\boldsymbol{\omega}}(G_{\boldsymbol{\theta}}(\mathbf{z}, \mathbf{y}), \mathbf{y})]
+ \lambda_{gp} \cdot \mathbb{E}_{\hat{\mathbf{x}}, \mathbf{y}} \left[(\|\nabla_{\hat{\mathbf{x}}} C_{\boldsymbol{\omega}}(\hat{\mathbf{x}}, \mathbf{y})\|_{2} - 1)^{2} \right]
+ \lambda \cdot \mathbb{E}_{\mathbf{x}, \mathbf{y}}[\|P(\mathbf{x}, \mathbf{y}) - P(G_{\boldsymbol{\theta}}(\mathbf{0}|\mathbf{y}), \mathbf{y})\|_{2}^{2}]$$
(3)

where $\hat{\mathbf{x}}$ indicates a uniform sample on the straight lines between \mathbf{x} and \mathbf{g}_{θ} . The generator function G_{θ} and the critic function C_{ω} are both implemented in deep neural networks, as will be detailed in the next section.

B. Neural networks structures

Fig. 1a presents the detailed structure of the LAG-based generator. We adopt the residual network from EDSR [39] as a basic downscaling block for its lightweight and efficiency, then grow it under the LAG framework using the progressive training strategy of ProGAN [37] to achieve a larger scaling factor. Each downscale block in the generator consists of a $2\times$ nearest neighbor interpolation layer and two convolution

layers with the Leaky ReLU activation function separately. The critic uses a similar structure as the generator but in reverse order as shown in Fig. 1b. The nearest neighbor interpolation layer in the downscale block of the generator is replaced by a new layer, which moves space to channels to turn downscale blocks into upscale blocks.

With the progressive training strategy of ProGAN, new downscale and upscale blocks can be systematically added to both the generator and discriminator networks, and ensure all layers trainable and stable across the entire training process. It is worthy noting that there is an extra transition phase that occurs before the training progresses smoothly incorporates the newly added layers by increasing their weights from 0 to 1. The transition phase is irreplaceable in avoiding sudden changes in image resolution; see [37] for more information.

IV. EXPERIMENTAL DESIGN

To highlight the advantages of the described LAG-based downscaling framework for stochastic extreme downscaling, we applied the method to downscale gridded climate datasets and compared the performances with the current state-of-the-art methods from both quantitative and qualitative perspectives. The characteristics and advantages of the LAG-based model, such as model uncertainty and mass-preservation, were also examined. All the codes (in Python) and pretrained weights are available at https://github.com/LiGuiye/LAG_Climate.

A. Datasets

The datasets we used are gridded data of wind velocity and solar irradiance covering the continental United States. The datasets were obtained from National Renewable Energy Laboratory's (NREL's) Wind Integration National Database (WIND) Toolkit [62] and National Solar Radiation Database (NSRDB) [63]. Examples of the two gridded datasets are given in Fig. 4 and 5 in the next section. As can be observed from the data, the solar irradiance dataset exhibits more complex patterns than the wind velocity dataset. Both datasets have been used as a benchmark for evaluating downscaling methods [13], [51].

The WIND Toolkit provides 4-hourly data on a uniform 2-km grid. We chose the 100-meter height wind speed and direction data points and converted them into easterly (u) and northerly (v) wind velocities as two different image channels. Data points were collected from 2007 to 2014 within a randomly selected 1,024 square kilometer area of the continental United States. The NSRDB contains half-hourly measurements for Direct Normal Irradiance (DNI) and Diffuse Horizontal Irradiance (DHI) at 4-km spatial resolution in latitude and longitude. DNI and DHI are the amounts of solar radiation received per unit area that reaches the earth directly and indirectly from the sun. We sampled the data hourly during daylight hours (from 6 AM to 6 PM) from 2007 to 2014 for data quality and diversity.

The chosen wind velocity and solar irradiance data were mapped to gridded images (with image size 512×512) and chronologically split into training and testing datasets. The

TABLE I
DETAILS OF THE TRAINING AND TESTING DATASETS.

Dataset	Wind velocity	Solar irradiance		
Years Spatial resolution Temporal resolution	2007 - 2014 2 km 4-hourly	$2007-2014$ $4~\mathrm{km}$ hourly		

datasets from 2007 to 2013 were used for training, and the ones from 2014 were used for testing. The training sets of wind velocity and solar irradiance data contain 46,026 and 30,056 images, respectively. The test sets include 5,605 wind velocity grids and 3,648 solar irradiance grids. Table I summarizes the details of the datasets.

B. Training details

The HR images in the training datasets (with image size 512×512) were first upscaled to LR image sizes (8×8) using average pooling. The upscaled (LR) images (y) and original HR images (x) were for training the model. We employed an Adam optimizer [64] with $\alpha_1=0, \ \alpha_2=0.99, \ \text{and} \ \epsilon=1e^{-8}$ for optimization and an exponential moving average with a decay of 0.999 was used for the weights of the generator for better visual effects. The generator and critic used the same learning rate, and we trained the critic functions more times than the generator for better results.

Models for wind velocity and solar irradiance data were trained separately using 1 NVIDIA A100 GPU. For the wind velocity data, we trained the model 30 epochs for each transition and stabilization phase at different resolutions with a batch size of 16 and a learning rate of 2×10^{-3} . For the solar irradiance data, we found that smaller batch sizes helped to improve the model performance during the evaluation process, possibly due to the heterogeneity of the images. We used a batch size of 1 and a learning rate of 4×10^{-3} to train the model for 15 epochs at each transition and stabilization phase.

C. Accuracy metrics

Similar to the training process, during testing, we upscaled the HR images in the testing dataset as the model inputs, and used the original HR images as references. We used relative Mean Squared Error (MSE) and Sliced Wasserstein Distance (SWD) [65] to measure the discrepancy between the generated images of the LAG-based method with reference images. The relative MSE, MSE divided by the average value in ground truth images, measures the pixel-wise accuracy, while the SWD, a variant of Wasserstein Distance or Earth-Mover distance [66], [67], measures the perceptual accuracy. For SWD, we adopted the same calculation methods as used in ProGAN [68], first normalizing each channel and then computing the mean value of SWDs across all channels.

Furthermore, we used semivariograms to evaluate the performance of each method in reproducing spatial patterns. As mentioned previously, the semivariogram is a commonly used geostatistical tool to measure the spatial variations of spatial measurements [69], [70]. Despite being a two-point statistics, it provides further insights on how measurements

TABLE II

ACCURACY STATISTICS COMPARISON OF GENERATION PERFORMANCE OF DIFFERENT MODELS. MODELS WITH BOLD VALUES OUTPERFORM OTHER MODELS ON THIS METRIC AT THE CURRENT SCALING FACTOR.

Wind velocity	relative MSE (\downarrow) / SWD (\downarrow)						
	ATPK	DIP	EDSR	ESRGAN	PhIRE GAN	LAG (our)	
4×	0.505/0.167	0.898/0.158	0.261/0.124	0.391/0.145		0.278/0.124	
8×	0.660/0.170	1.886/0.168				0.460/0.122	
$50 \times$					0.940/0.162		
$64 \times$						0.936/0.107	
Solar irradiance	ATPK	DIP	EDSR	ESRGAN	PhIRE GAN	LAG (our)	
4×	0.145/0.199	0.090/0.184	0.090/0.164	0.138/0.197		0.081/0.158	
8×	0.173/0.200	0.126 /0.195	,	,		0.128/ 0.151	
$25 \times$	0.268/0.217	0.402/0.415			0.135/0.136		
$32 \times$	·				,	0.251/0.130	
$64 \times$						0.299/0.123	

vary over the space. Datasets with comparable spatial patterns are expected to have closely aligned semivariograms, reflecting similar spatial continuity and variability.

D. Model comparisons

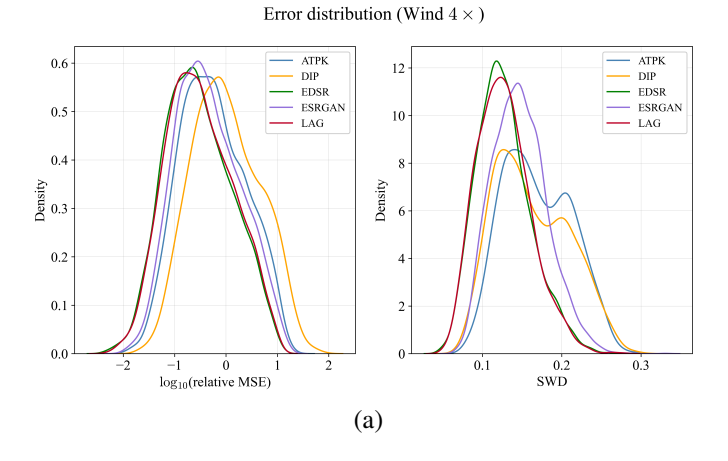
For a comprehensive comparison, we selected five models of three types: traditional geostatistical methods, unsupervised methods for image super-resolution, and GAN-based methods. These methods include Area-to-point (ATP) kriging [25], [26], Deep Image Prior (DIP) [38], EDSR [39], ESRGAN [31], and PhIRE GAN [13]. The performances of these methods were compared at different scaling factors (from $4 \times$ to $64 \times$) with the above mentioned reference datasets. For fairness of comparison, the GAN-based methods were evaluated at respective scaling factors that they were originally optimized for. For instance, the EDSR and ESRGAN models were originally designed for $4 \times SR$ and hence were only compared at $4\times$ in this study. For PhIRE GAN, it used a two-step process and can perform 50× SR for the wind velocity and 25× SR for the solar irradiance data. The pre-trained weights from https://github.com/NREL/PhIRE were used to generate test samples for comparison [71]. For DIP, the original method was initially optimized for $4\times$ and $8\times$ SR. For ATPK, we only applied it up to $10 \times SR$ due to the decreasing performances.

V. RESULTS

A. Accuracy statistics

We applied the trained models to downscale the upscaled wind velocity and solar irradiance test datasets and collected the accuracy statistics by comparing the downscaled results with the reference data. Table II shows the median relative MSE and SWD values of the compared methods at different scaling factors for wind velocity and solar irradiance test data. Smaller values indicate better performances. Blank entries means the methods were not performed at the associated scaling factors for the reasons discussed above.

For wind velocity data with small scaling factors like $4\times$ (image size increases from 8×8 to 32×32), EDSR and LAG achieved a comparable level of accuracy, both outperforming the other methods in comparison. For solar irradiance data



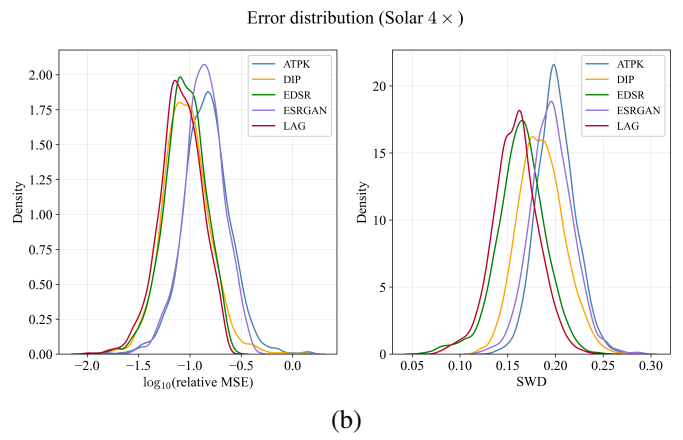


Fig. 2. Empirical density distribution of the relative MSE (in logarithmic scale) and SWD across (a) wind velocity and (b) solar irradiance test datasets of different models at 4× SR scale. For the wind velocity data, EDSR outperforms other models, and LAG achieves comparable results. For the solar irradiance data, LAG outperforms other models.

with more complex patterns, LAG achieved the best accuracy at $4\times$ SR. With the increase in scaling factor ($8\times$, $32\times$ and $64\times$), the SWD metrics for LAG remains stable, whereas the relative MSE exhibits an increasing trend. Nonetheless LAG still outperformed other methods evaluated.

Fig. 2 shows the empirical density distribution of the relative MSE (in logarithmic scale) and SWD across the wind velocity

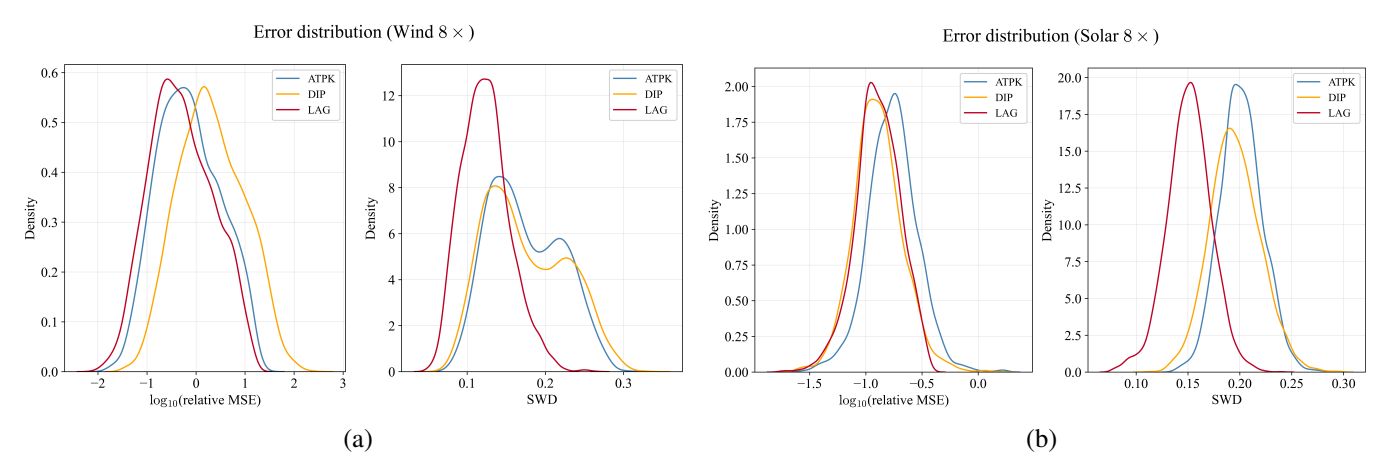


Fig. 3. Empirical density distribution of the relative MSE (in logarithmic scale) and SWD across (a) wind velocity and (b) solar irradiance test datasets of different models at $8 \times$ SR scale. LAG outperforms other models.

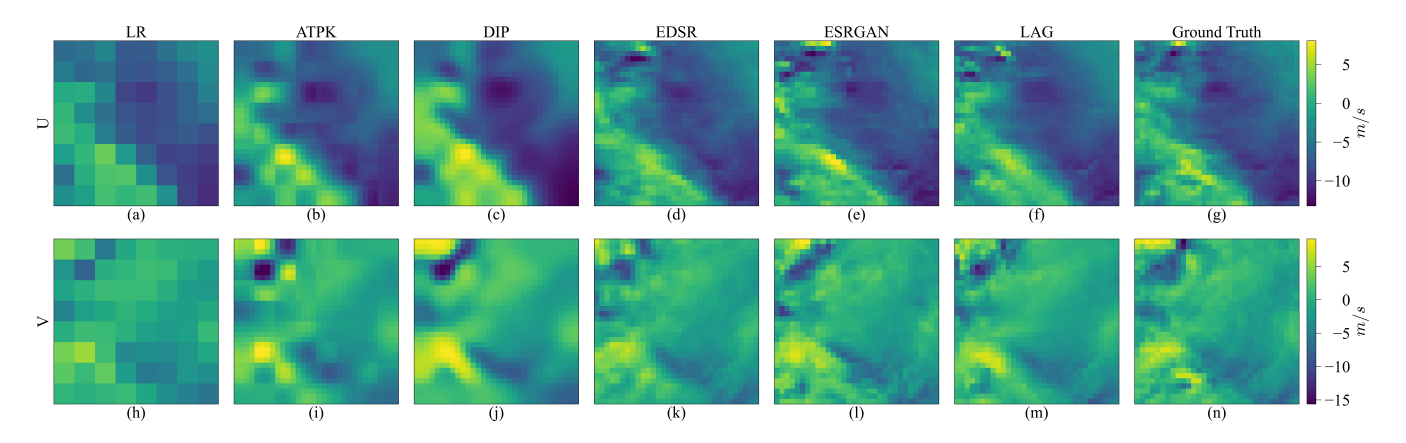


Fig. 4. $4 \times SR$ results generated by different methods for two channels (U and V) of a randomly sampled LR image from the wind velocity test dataset. The leftmost column [(a) and (h)] shows the input LR images at two channels (with image size 8×8), the rightmost column [(g) and (n)] shows the corresponding HR ground truth images (with image size 32×32). The columns in between shows the results of the compared methods.

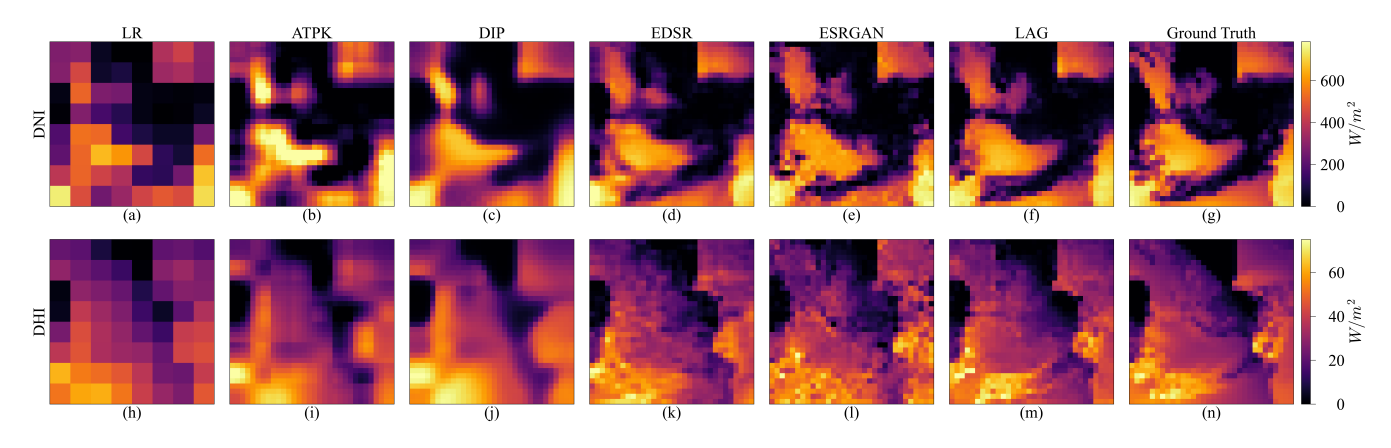


Fig. 5. $4 \times$ SR results generated by different methods for two channels (*DNI* and *DHI*) of a randomly sampled LR image from the solar radiance test dataset. The leftmost column [(a) and (h)] shows the input LR images at two channels (with image size 8×8), the rightmost column [(g) and (n)] shows the corresponding HR ground truth images (with image size 32×32). The columns in between shows the results of the compared methods.

and solar irradiance test datasets of different models at $4 \times$ scale. Similar as in Table II, LAG generates comparable results with the best model EDSR on the wind velocity data. ESRGAN performs better than DIP and ATPK. LAG outperforms other models for the solar irradiance data with more complex and heterogeneous spatial patterns.

As the scaling factor increases, the advantages of our model become more obvious; see Fig. 3 for the comparison of $8\times$ results. Since most other methods are not initially designed for large scaling factors, we only represent comparison plots at $4\times$ and $8\times$ scales. More plots of error distribution at different SR scales can be seen in the Supplementary Material.

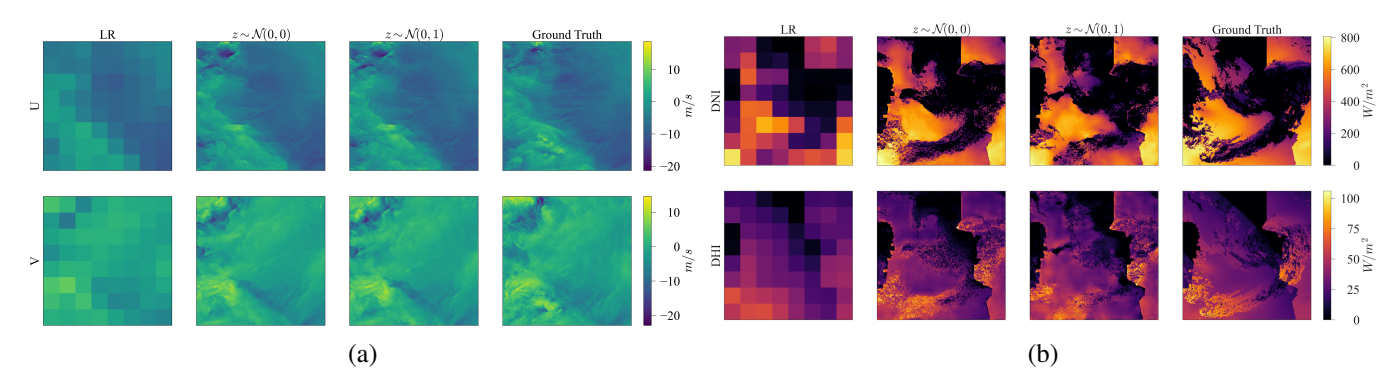


Fig. 6. $64 \times$ SR results generated by the LAG-based downscaing framework for a randomly sampled LR image from (a) wind velocity and (b) solar irradiance test datasets. For each panel, the leftmost column shows the input LR images at two channels (with image size 8×8), the rightmost column shows the corresponding HR ground truth images (with image size 512×512), and the columns in between shows results of LAG.

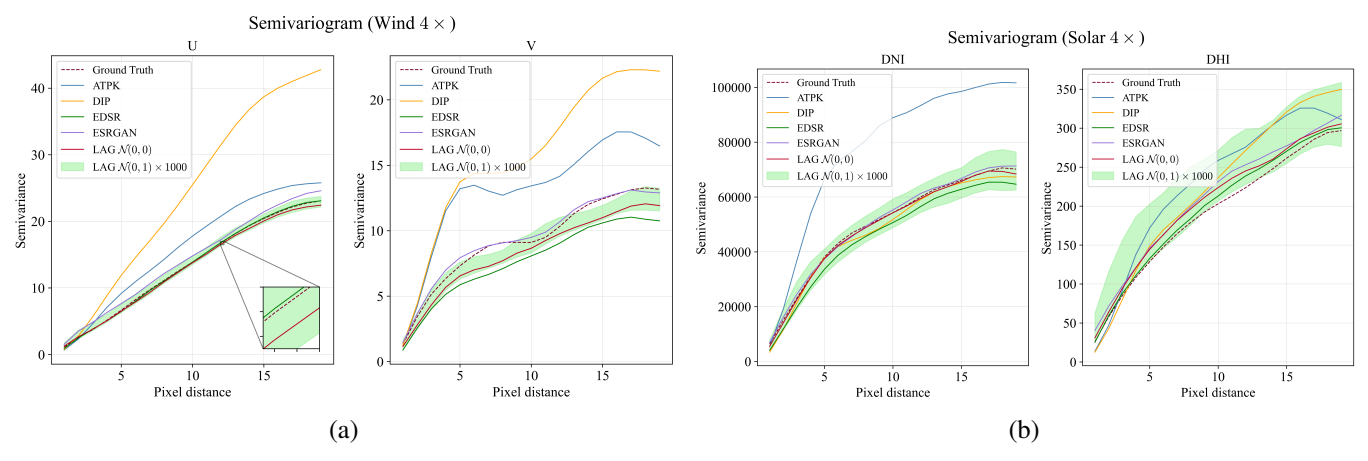


Fig. 7. Semivariograms of the $4\times$ SR results generated by different models for a randomly sampled LR image from (a) wind velocity and (b) solar irradiance test datasets. Images with similar spatial patterns should have close lines. The red solid line labeled as "LAG $\mathcal{N}(0,0)$ " represents the semivariogram of the generated image at the center $G(\mathbf{0},\mathbf{y})$. The green envelope indicates the empirical interval of the semivariograms of 1000 realizations randomly generated by the LAG-based method with $\mathbf{z} \sim \mathcal{N}(\mathbf{0},\mathbf{1})$ indicating the model uncertainty.

B. Visual analysis

We randomly selected one image from both the wind velocity and solar irradiance test datasets (both with two channels) and compared the performances of the methods in reproducing the spatial patterns in the reference data.

Figs. 4 and 5 show the $4\times$ SR results generated by the compared methods for the wind velocity and solar irradiance datasets, respectively. The leftmost column indicates the input LR images (with image size 8×8) randomly sampled from the test set, while the rightmost column shows the corresponding HR ground truth images (with image size 32×32). The results of different methods are shown in the columns in between (all with image size 32×32). As one can see, EDSR and the GANbased methods including LAG and ESRGAN generated much closer results to the ground truth. In contrast ATPK and DIP resulted in overly smoothed images with losses of the fine details. It is expected considering DIP is unsupervised and ATPK only considers two-point statistics. While the results of LAG, EDSR and ESRGAN are visually comparable for wind velocity images (Fig. 4), LAG produced overall best results for the solar irradiance data with more heterogeneity in spatial patterns (Fig. 5). These are consistent with the accuracy statistics in Section V-A. Fig. 6 shows the $64 \times$ LAG SR results for the wind velocity and solar irradiance data. As one can see, even at this large scaling factor, the LAG method can effectively reproduce impressively fine details in the reference images. We have included more test results at different scaling factors in the Supplementary Material.

Fig. 7 shows the semivariograms of the ground truth image and the corresponding HR images generated by different models at scaling factor 4 for a randomly sampled LR image from the wind velocity and solar irradiance test datasets. The green envelope represents the empirical interval of the semivariograms of 1000 realizations produced by the LAGbased method with $\mathbf{z} \sim \mathcal{N}(\mathbf{0}, \mathbf{1})$. As one can see in Fig. 7, EDSR and two GAN-based methods (LAG and ESRGAN) produced closer semivariograms to that of the ground truth than DIP and ATPK, indicating that they well reproduced the spatial patterns of the ground truth data at $4\times$ scaling factor. Among the three outperforming methods, one can see the semivariogram of LAG result is overall the closest to that of the ground truth. This is consistent with the previous visual checking results. Fig. 8 compares the semivariograms of LAG and PhIRE GAN results at 64× scaling factor for a randomly sampled LR image from the wind velocity and solar irradiance

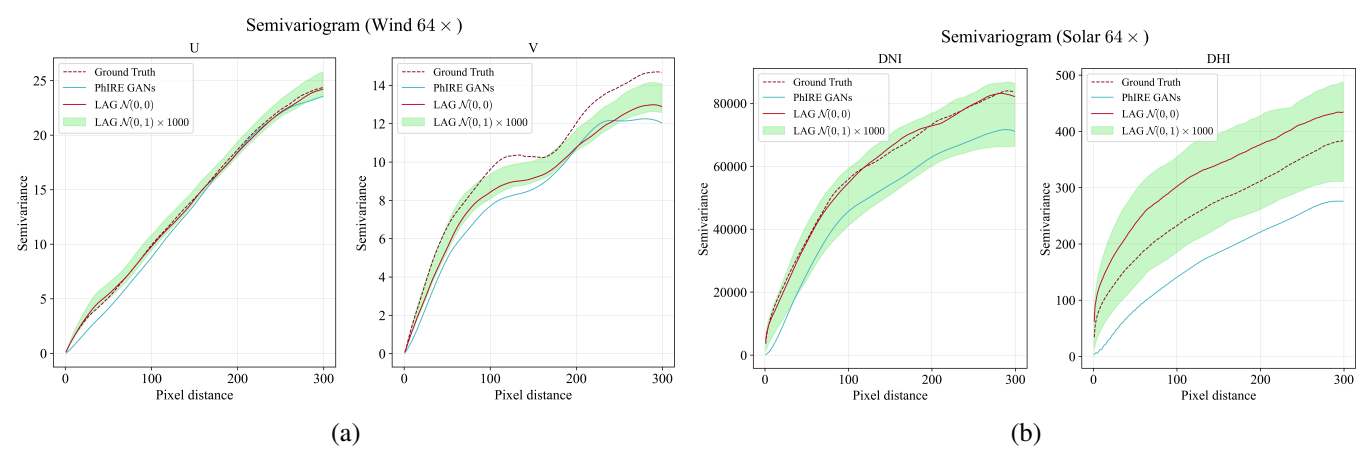


Fig. 8. Semivariograms of the $64 \times SR$ results generated by the LAG-based method and the PhIRE GAN for a randomly sampled LR image from (a) wind velocity and (b) solar irradiance test datasets. Images with similar spatial patterns should have close lines. The red solid line labeled as "LAG $\mathcal{N}(0,0)$ " represents the semivariogram of the generated image at the center $G(\mathbf{0},\mathbf{y})$. The green envelope indicates the empirical interval of the semivariograms of 1000 realizations randomly generated by the LAG-based method with $\mathbf{z} \sim \mathcal{N}(\mathbf{0},\mathbf{1})$ indicating the model uncertainty.

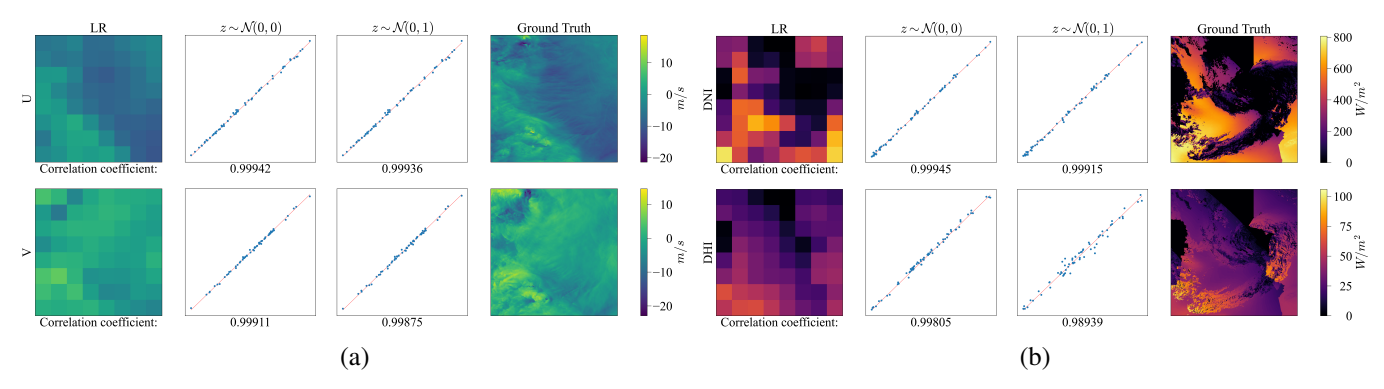


Fig. 9. Consistency check for the $64 \times$ SR results generated by the LAG-based method for a randomly sampled LR image from (a) wind velocity and (b) solar irradiance test datasets. A random realization of LAG ($\mathbf{z} \sim \mathcal{N}(\mathbf{0}, \mathbf{1})$) was used to generate the scatter plots. The horizontal axis represents the pixel values in the input LR image and vertical axis represents the average of the associated 64×64 pixel values. Scatter points align well with the 45-degree (red solid) line. The Pearson correlation coefficients (listed in the bottom) are all close to 1.

test datasets. Note PhIRE GAN performed $50\times$ SR for wind velocity and $25\times$ SR for solar irradiance datasets. It is obvious that the semivariograms of LAG is closer to that of the ground truth. More semivariogram plots at different scaling factors are given in the Supplementary Material.

C. Mass preservation

As mentioned, preserving mass is important for successful scientific downscaling methods. To check the consistency of LAG results, we show scatter plots between the original pixel values and the average of associated pixel values in LAG $64\times$ SR outcomes (image generated with $\mathbf{z}=0$ and a randomly selected image generated with $\mathbf{z}\sim\mathcal{N}(\mathbf{0},\mathbf{1})$) (see Fig. 9). In the downscaling process with $64\times$ scaling factor, one pixel in an LR image will be refined into 64×64 pixels. The horizontal axis of each plot represents the pixel values of the input LR image, and the vertical axis represents the average values of the corresponding 64×64 pixels in the resultant HR images. We can see that the scatter points align well with the 45° straight line, suggesting a high degree of consistency between the values of LR pixels and the average of HR pixels. This

can also be confirmed by the Pearson correlation coefficients shown in the bottom of each plot, all of which are close to 1.

D. Uncertainty characterization

In traditional statistics, the uncertainty of high-dimensional distributions is often examined through Monte Carlo stochastic simulations. This approach involves the generation of numerous random samples from the distribution to approximate and analyze the statistical properties of interest, allowing for the assessment of uncertainty and robustness of complex distributions in an empirical fashion. Similarly, we can leverage the LAG's ability in producing repeated plausible HR images for a downscaling task to empirically characterize the uncertainty of LAG outcomes.

Fig. 10 shows the maps of empirical mean (second column) and standard deviation (third column) for the $64\times$ SR results of randomly sampled LR images (first column) in (a) wind velocity and (b) solar irradiance test datasets. The statistics were derived based on 1000 realizations of the trained LAG model with $\mathbf{z} \sim \mathcal{N}(\mathbf{0},\mathbf{1})$. One can see the estimations with higher standard deviation tend to happen in the edge areas with

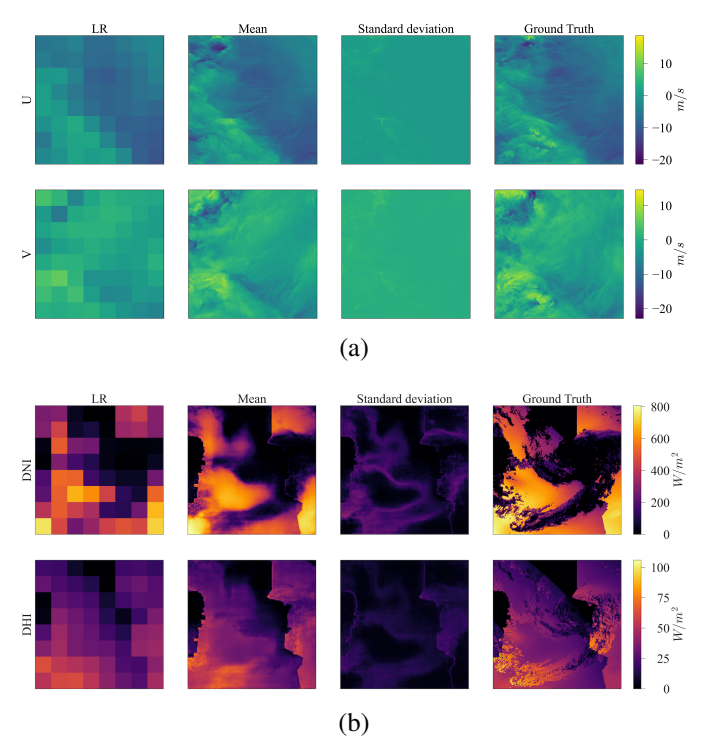
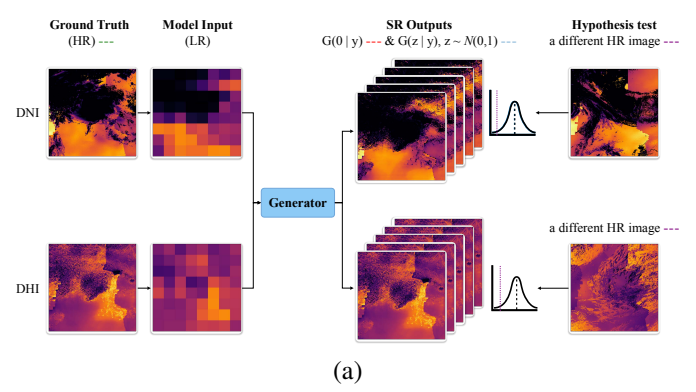


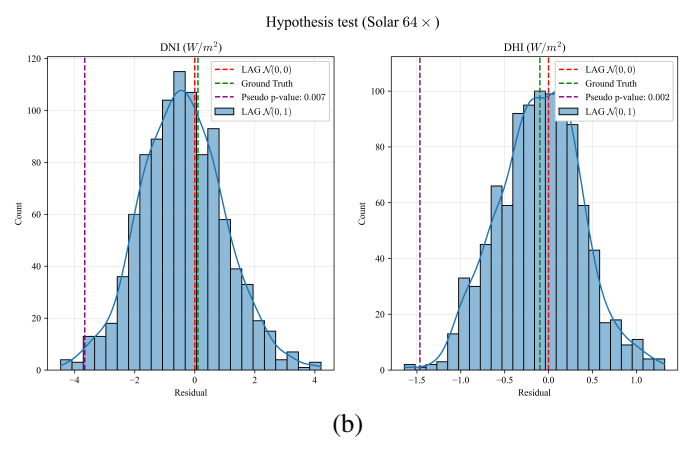
Fig. 10. Empirical mean (second column) and standard deviation (third column) images based on the 1000 random realizations generated by LAG with $\mathbf{z} \sim \mathcal{N}(\mathbf{0},\mathbf{1})$ for a randomly sampled LR image from (a) wind velocity and (b) solar irradiance test datasets. For each panel, the leftmost column shows the input LR images at two channels (with image size 8×8), the rightmost column shows the corresponding HR ground truth images (with image size 512×512).

rapid pixel value changes. The standard deviations for solar irradiance data tend to be higher than that for wind velocity. This can be due to the more complex and heterogeneous spatial patterns in the solar irradiance data. This can also be verified by the semivariogram plots in Figs. 7 and 8, where the interval envelopes for solar irradiance data are much wider than those of wind velocity, indicating higher degree of uncertainty in the trained models for solar irradiance data.

We can leverage the simulation-based approach for further statistical inferences. For instance, one can quantify the variation among the random realizations by assessing their divergence from the central tendency of the latent distribution $G(\mathbf{0}|\mathbf{y})$. This divergence can be measured using metrics such as residuals, MSE or SWDs. The distribution of the divergence can not only provides further empirical evidences about the model biases and uncertainty, but also facilitates statistical inferences. For example, it allows one to perform hypothesis testing to check if a given HR image could plausibly be a downscaled outcome of a LR image given the information learned in LAG.

Fig. 11 illustrates the process of hypothesis testing with the solar irradiance test dataset. Fig. 11a shows the input LR (with two channels DNI and DHI), related ground truth images and several random realizations from the trained LAG model. Figs. 11b and 11c show the empirical distribution of the discrepancy between each of 1,000 realizations from the latent distribution center $G(\mathbf{0}|\mathbf{y})$ (red dashed line). Given an example HR image (the rightmost in Fig. 11a), we can calculate its





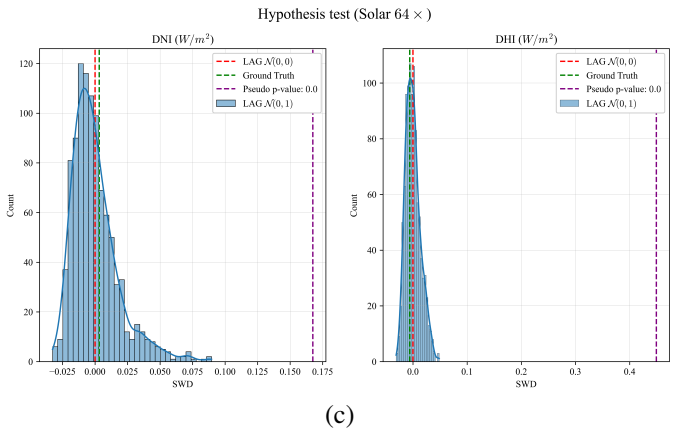


Fig. 11. An illustration of the LAG-based hypothesis testing process using the solar irradiance data (with two channels DNI and DHI) with $64\times$ scaling factor: (a) shows the diagram of the hypothesis testing process; (b) and (c) are the empirical distributions of the discrepancy of the 1000 random realizations from the distribution center (red dashed line) measured in residuals and SWD, respectively. The purple dash line indicates the measure of the HR image to be tested.

discrepancy to the center in terms of residuals or SWD, based on which a psuedo p-value can be derived to statistically test if the given image is a plausible outcome of the LR image. The pseudo p-value is small enough to significantly reject the hypothesis the given HR image is a plausible downscaled outcome of the LR image. While this example used residuals and SWD to illustrate the concept, it is important to note that other measures of image discrepancy or similarity measures can also be applied to evaluate the relationship between HR and LR images.

VI. CONCLUSION AND DISCUSSIONS

In this study, we described a LAG-based method for extreme stochastic downscaling for gridded scientific datasets. As a variant of conditional GAN, the LAG method addressed the specific requirements in scientific downscaling, including uncertainty characterization and downscaling with high scaling factors. Compared to existing GAN methods, LAG can explicitly account for the stochasticity in one-to-many mappings inherent to the downscaling process. LAG was implemented with progressing GAN framework to avoid mode collapse when dealing with high scaling factor. For a given LR image, LAG allows for generating a multitude of plausible downscaling outcomes instead of producing deterministic results. We showcased the advantages of the LAG method with a case study of downscaing gridded climate datasets and highlighted its performances with a comprehensive compression with commonly used downscaling methods developed from different perspectives, including ATPK, DIP, EDSR, ESRGAN, and PhIRE GAN. Furthermore, we checked the mass consistency of the LAG output and examined the uncertainty spaces through simulation-based Monte Carlo approach.

Future improvements of the method are envisioned in two directions. First, we plan to extend the developed down-scaling method to spatiotemporal settings, which allows for the generation of time series of gridded datasets with very spatial and temporal resolution. This requires the method to not only effectively consider the complex spatial patterns but also temporal dynamics in the measurements. Secondly, the stochastic nature of the LAG allows for the empirical exploration of the uncertainty space. While this empirical approach has proven effective, it remains challenging to adequately incorporate domain knowledge into the modeling process. We plan to address this by integrating the LAG with a Bayesian framework [72], which is known for its versatility in incorporating prior knowledge in uncertainty modeling.

ACKNOWLEDGMENTS

The authors gratefully acknowledge the funding support provided by National Science Foundation (BCS: #2026331). This work utilized the Alpine high performance computing resource at the University of Colorado Boulder. Alpine is jointly funded by the University of Colorado Boulder, the University of Colorado Anschutz, Colorado State University, and the National Science Foundation (BCS: #2201538).

REFERENCES

- [1] P. N. Edwards, "History of climate modeling," Wiley Interdisciplinary Reviews: Climate Change, vol. 2, no. 1, pp. 128–139, Jan. 2011.
- [2] J. T. Overpeck, G. A. Meehl, S. Bony, and D. R. Easterling, "Climate data challenges in the 21st century," *science*, vol. 331, no. 6018, pp. 700–702, 2011.
- [3] G. J.-P. Schumann and P. D. Bates, "The need for a high-accuracy, open-access global digital elevation model," p. 618194, 2020.
- [4] M. Ekström, M. R. Grose, and P. H. Whetton, "An appraisal of downscaling methods used in climate change research," Wiley Interdisciplinary Reviews: Climate Change, vol. 6, no. 3, pp. 301–319, 2015.
- [5] B. C. Hewitson and R. G. Crane, "Climate downscaling: techniques and application," *Climate Research*, vol. 7, no. 2, pp. 85–95, 1996.
- [6] N. A. Cressie, "Change of support and the modifiable areal unit problem," Geographical Systems, 1996.

- [7] M. F. Goodchild, L. Anselin, and U. Deichmann, "A framework for the areal interpolation of socioeconomic data," *Environment and planning* A, vol. 25, no. 3, pp. 383–397, Mar. 1993.
- [8] Y. LeCun, Y. Bengio, and G. Hinton, "Deep learning," *Nature*, vol. 521, no. 7553, pp. 436–444, 2015.
- [9] W. Yang, X. Zhang, Y. Tian, W. Wang, J.-H. Xue, and Q. Liao, "Deep learning for single image super-resolution: A brief review," *IEEE Transactions on Multimedia*, vol. 21, no. 12, pp. 3106–3121, Dec. 2019.
- [10] Z. Wang, J. Chen, and S. C. H. Hoi, "Deep learning for image superresolution: A survey," *IEEE Transactions on Pattern Analysis and Machine Intelligence*, vol. 43, no. 10, pp. 3365–3387, Oct. 2021.
- [11] K. Chauhan, S. N. Patel, M. Kumhar, J. Bhatia, S. Tanwar, I. E. Davidson, T. F. Mazibuko, and R. Sharma, "Deep Learning-Based Single-Image Super-Resolution: A Comprehensive Review," *IEEE Access*, vol. 11, pp. 21811–21830, 2023.
- [12] S. Jozdani, D. Chen, D. Pouliot, and B. A. Johnson, "A review and meta-analysis of generative adversarial networks and their applications in remote sensing," *International Journal of Applied Earth Observation* and Geoinformation, vol. 108, p. 102734, Apr. 2022.
- [13] K. Stengel, A. Glaws, D. Hettinger, and R. N. King, "Adversarial superresolution of climatological wind and solar data," *Proceedings of the National Academy of Sciences*, vol. 117, no. 29, pp. 16805–16815, Jul. 2020.
- [14] J. Leinonen, D. Nerini, and A. Berne, "Stochastic Super-Resolution for Downscaling Time-Evolving Atmospheric Fields With a Generative Adversarial Network," *IEEE Transactions on Geoscience and Remote* Sensing, vol. 59, no. 9, pp. 7211–7223, Sep. 2021.
- [15] M. F. Goodchild, "How well do we really know the world? uncertainty in giscience," *Journal of Spatial Information Science*, no. 20, pp. 97–102, 2020.
- [16] G. Cao, "Deep learning of big geospatial data: Challenges and opportunities," New Thinking in GIScience, pp. 159–169, 2022.
- [17] J. Postels, H. Blum, C. Cadena, R. Siegwart, L. Van Gool, and F. Tombari, "Quantifying aleatoric and epistemic uncertainty using density estimation in latent space," arXiv preprint arXiv:2012.03082, vol. 1, 2020.
- [18] A. Tarantola, Inverse Problem Theory and Methods for Model Parameter Estimation. Society for Industrial and Applied Mathematics, Jan. 2005.
- [19] M. Abdar, F. Pourpanah, S. Hussain, D. Rezazadegan, L. Liu, M. Ghavamzadeh, P. Fieguth, X. Cao, A. Khosravi, U. R. Acharya, V. Makarenkov, and S. Nahavandi, "A review of uncertainty quantification in deep learning: Techniques, applications and challenges," *Information Fusion*, vol. 76, pp. 243–297, Dec. 2021.
- [20] D. J. MacKay, "A practical bayesian framework for backpropagation networks," *Neural computation*, vol. 4, no. 3, pp. 448–472, 1992.
- [21] A. G. Wilson, "The case for bayesian deep learning," arXiv preprint arXiv:2001.10995, 2020.
- [22] B. Lakshminarayanan, A. Pritzel, and C. Blundell, "Simple and scalable predictive uncertainty estimation using deep ensembles," *Advances in neural information processing systems*, vol. 30, 2017.
- [23] R. Rahaman et al., "Uncertainty quantification and deep ensembles," Advances in Neural Information Processing Systems, vol. 34, pp. 20063–20075, 2021.
- [24] W. R. Tobler, "Smooth pycnophylactic interpolation for geographical regions," *Journal of the American Statistical Association*, vol. 74, no. 367, pp. 519–530, 1979.
- [25] P. C. Kyriakidis, "A geostatistical framework for area-to-point spatial interpolation," *Geographical Analysis*, vol. 36, no. 3, pp. 259–289, 2004.
- [26] P. C. Kyriakidis and E.-H. Yoo, "Geostatistical prediction and simulation of point values from areal data," *Geographical Analysis*, vol. 37, no. 2, pp. 124–151, 2005.
- [27] P. M. Atkinson, "Downscaling in remote sensing," *International Journal of Applied Earth Observation and Geoinformation*, vol. 22, pp. 106–114, Jun. 2013.
- [28] I. Goodfellow, J. Pouget-Abadie, M. Mirza, B. Xu, D. Warde-Farley, S. Ozair, A. Courville, and Y. Bengio, "Generative adversarial networks," *Communications of the ACM*, vol. 63, no. 11, pp. 139–144, Oct. 2020.
- [29] M. Mirza and S. Osindero, "Conditional generative adversarial nets," arXiv preprint arXiv:1411.1784, 2014.
- [30] C. Ledig, L. Theis, F. Huszár, J. Caballero, A. Cunningham, A. Acosta, A. Aitken, A. Tejani, J. Totz, Z. Wang et al., "Photo-realistic single image super-resolution using a generative adversarial network," in Proceedings of the IEEE conference on computer vision and pattern recognition, 2017, pp. 4681–4690.
- [31] X. Wang, K. Yu, S. Wu, J. Gu, Y. Liu, C. Dong, Y. Qiao, and C. Change Loy, "Esrgan: Enhanced super-resolution generative adversar-

- ial networks," in *Proceedings of the European conference on computer vision (ECCV) workshops*, 2018, pp. 0–0.
- [32] B. Lim, S. Son, H. Kim, S. Nah, and K. M. Lee, "Enhanced Deep Residual Networks for Single Image Super-Resolution," in *IEEE Com*puter Society Conference on Computer Vision and Pattern Recognition Workshops, 2017.
- [33] J. Leinonen, A. Guillaume, and T. Yuan, "Reconstruction of Cloud Vertical Structure With a Generative Adversarial Network," *Geophysical Research Letters*, vol. 46, no. 12, pp. 7035–7044, Jun. 2019.
- [34] X. Jiang, X. Wang, Y. Liu, E. J. M. Carranza, S. Xie, and X. Wan, "Spatial extrapolation of downscaled geochemical data using conditional GAN," *Computers & Geosciences*, vol. 179, p. 105420, Oct. 2023.
- [35] D. Yang, S. Hong, Y. Jang, T. Zhao, and H. Lee, "Diversity-Sensitive Conditional Generative Adversarial Networks," Jan. 2019.
- [36] D. Berthelot, P. Milanfar, and I. Goodfellow, "Creating high resolution images with a latent adversarial generator," arXiv preprint arXiv:2003.02365, 2020.
- [37] T. Karras, T. Aila, S. Laine, and J. Lehtinen, "Progressive growing of gans for improved quality, stability, and variation," arXiv preprint arXiv:1710.10196, 2017.
- [38] D. Ulyanov, A. Vedaldi, and V. Lempitsky, "Deep image prior," in Proceedings of the IEEE conference on computer vision and pattern recognition, 2018, pp. 9446–9454.
- [39] B. Lim, S. Son, H. Kim, S. Nah, and K. Mu Lee, "Enhanced deep residual networks for single image super-resolution," in *Proceedings* of the IEEE conference on computer vision and pattern recognition workshops, 2017, pp. 136–144.
- [40] N. A. Cressie, "Change of Support and the Modifiable Areal Unit Problem," Geographical Systems, vol. 3, pp. 159–180, 1996.
- [41] C. A. Gotway and L. J. Young, "Combining incompatible spatial data," Journal of the American Statistical Association, vol. 97, no. 458, pp. 632–648, 2002.
- [42] S. Openshaw and P. J. Taylor, "A million or so correlation coefficients: Three experiments on the modifiable areal unit problem," *Statistical applications in the spatial sciences*, pp. 127–144, 1979.
- [43] M. F. Goodchild, "The Openshaw effect," International Journal of Geographical Information Science, vol. 0, no. 0, pp. 1–2, Jul. 2022.
- [44] E. Pardo-Igúzquiza, M. Chica-Olmo, and P. M. Atkinson, "Downscaling cokriging for image sharpening," *Remote Sensing of Environment*, vol. 102, no. 1-2, pp. 86–98, 2006.
- [45] P. M. Atkinson, E. Pardo-Iguzquiza, and M. Chica-Olmo, "Downscaling cokriging for super-resolution mapping of continua in remotely sensed images," *IEEE Transactions on Geoscience and Remote Sensing*, vol. 46, no. 2, pp. 573–580, Feb. 2008.
- [46] Q. Wang, W. Shi, P. M. Atkinson, and Y. Zhao, "Downscaling modis images with area-to-point regression kriging," *Remote Sensing of Envi*ronment, vol. 166, pp. 191–204, Sep. 2015.
- [47] Y. Tang, P. M. Atkinson, and J. Zhang, "Downscaling remotely sensed imagery using area-to-point cokriging and multiple-point geostatistical simulation," *ISPRS Journal of Photogrammetry and Remote Sensing*, vol. 101, pp. 174–185, Mar. 2015.
- [48] X. Zhang, H. Jiang, G. Zhou, Z. Xiao, and Z. Zhang, "Geostatistical interpolation of missing data and downscaling of spatial resolution for remotely sensed atmospheric methane column concentrations," *Interna*tional journal of remote sensing, vol. 33, no. 1, pp. 120–134, 2012.
- [49] G. Cao, "Deep Learning of Big Geospatial Data: Challenges and Opportunities," in *New Thinking in GIScience*. Singapore: Springer, 2022, pp. 159–169.
- [50] K. Singla, R. Pandey, and U. Ghanekar, "A review on Single Image Super Resolution techniques using generative adversarial network," *Optik*, vol. 266, p. 169607, Sep. 2022.
- [51] R. Kurinchi-Vendhan, B. Lütjens, R. Gupta, L. D. Werner, D. Newman, and S. Low, "WiSoSuper: Benchmarking Super-Resolution Methods on Wind and Solar Data," in *Climate Change AI*. Climate Change AI, Dec. 2021.
- [52] W. Yang, X. Zhang, Y. Tian, W. Wang, J.-H. Xue, and Q. Liao, "Deep Learning for Single Image Super-Resolution: A Brief Review," *IEEE Transactions on Multimedia*, vol. 21, no. 12, pp. 3106–3121, Dec. 2019.
- [53] K. Simonyan and A. Zisserman, "Very deep convolutional networks for large-scale image recognition," arXiv preprint arXiv:1409.1556, 2014.
- [54] Y. Bahat and T. Michaeli, "Explorable Super Resolution," in *Proceedings* of the IEEE/CVF Conference on Computer Vision and Pattern Recognition, 2020, pp. 2716–2725.
- [55] S. Menon, A. Damian, S. Hu, N. Ravi, and C. Rudin, "Pulse: Self-supervised photo upsampling via latent space exploration of generative models," in 2020 IEEE/CVF Conference on Computer Vision and Pattern Recognition (CVPR), Jun. 2020, pp. 2434–2442.

- [56] I. Goodfellow, J. Pouget-Abadie, M. Mirza, B. Xu, D. Warde-Farley, S. Ozair, A. Courville, and Y. Bengio, "Generative adversarial nets," Advances in neural information processing systems, vol. 27, 2014.
- [57] M. Arjovsky and L. Bottou, "Towards principled methods for training generative adversarial networks," arXiv preprint arXiv:1701.04862, 2017.
- [58] M. Arjovsky, S. Chintala, and L. Bottou, "Wasserstein generative adversarial networks," in *International conference on machine learning*. PMLR, 2017, pp. 214–223.
- [59] Y. Blau and T. Michaeli, "The Perception-Distortion Tradeoff," in Proceedings of the IEEE Conference on Computer Vision and Pattern Recognition, 2018, pp. 6228–6237.
- [60] M. Arjovsky, S. Chintala, and L. Bottou, "Wasserstein Generative Adversarial Networks," in *Proceedings of the 34th International Conference on Machine Learning*. PMLR, Jul. 2017, pp. 214–223.
- [61] I. Gulrajani, F. Ahmed, M. Arjovsky, V. Dumoulin, and A. C. Courville, "Improved Training of Wasserstein GANs," in *Advances in Neural Information Processing Systems*, vol. 30. Curran Associates, Inc., 2017.
- [62] C. Draxl, B. Hodge, A. Clifton, and J. McCaa, "Overview and meteorological validation of the wind integration national dataset toolkit," National Renewable Energy Lab.(NREL), Golden, CO (United States), Tech. Rep., 2015.
- [63] M. Sengupta, Y. Xie, A. Lopez, A. Habte, G. Maclaurin, and J. Shelby, "The national solar radiation data base (NSRDB)," *Renewable and sustainable energy reviews*, vol. 89, pp. 51–60, 2018.
- [64] D. P. Kingma and J. Ba, "Adam: A method for stochastic optimization," arXiv preprint arXiv:1412.6980, 2014.
- [65] J. Rabin, G. Peyré, J. Delon, and M. Bernot, "Wasserstein barycenter and its application to texture mixing," in Scale Space and Variational Methods in Computer Vision: Third International Conference, SSVM 2011, Ein-Gedi, Israel, May 29–June 2, 2011, Revised Selected Papers 3. Springer, 2012, pp. 435–446.
- [66] Y. Rubner, C. Tomasi, and L. J. Guibas, "The earth mover's distance as a metric for image retrieval," *International journal of computer vision*, vol. 40, no. 2, p. 99, 2000.
- [67] ——, "A metric for distributions with applications to image databases," in Sixth international conference on computer vision (IEEE Cat. No. 98CH36271). IEEE, 1998, pp. 59–66.
- [68] T. Karras, T. Aila, S. Laine, and J. Lehtinen, "Progressive growing of gans for improved quality, stability, and variation," arXiv preprint arXiv:1710.10196, 2018.
- [69] J. Chiles and A. Delfiner, "Geostatistics: Modelling spatial uncertainty: Wiley interscience," New York, 1999.
- [70] S. R. Sain, R. Furrer, and N. Cressie, "A spatial analysis of multivariate output from regional climate models," *The Annals of Applied Statistics*, pp. 150–175, 2011.
- [71] K. Stengel, A. Glaws, D. Hettinger, and R. N. King, code for "Adversarial super-resolution of climatological wind and solar data." GitHub. https://github.com/NREL/PhIRE. Deposited 3 April 2020.
- [72] A. G. Wilson, "The Case for Bayesian Deep Learning," arXiv, Jan. 2020.



Guiye Li received his B.S. in Geographic Information Science from Hubei University, Wuhan, China, in 2020. He is currently pursuing his Ph.D. degree in the Department of Geography at the University of Colorado Boulder. His research interests include deep learning, GeoAI, and geostatistics as well as the climate and environment applications.



Guofeng Cao is an Assistant Professor in the Department of Geography at the University of Colorado Boulder. He received his B.S. degree in Earth Sciences from Zhejiang University, Hangzhou, China, M.S. in Statistics and Ph.D. in Geography both from the University of California, Santa Barbara, CA, USA. His research interests include GeoAl/machine learning, geostatistics, remote sensing, big spatiotemporal data analytics, and the innovative applications in addressing challenges related to climate and environment changes.

Supplementary material for "Generative Adversarial Models for Extreme Downscaling of Climate Datasets"

Guiye Li and Guofeng Cao

APPENDIX

SUPPLEMENTARY MATERIAL

This supplementary material contains additional figures that complement the main article. Figs. 1 and 2 present SR results generated by the LAG-based downscaling framework, $G(\mathbf{0}|\mathbf{y})$, for a randomly sampled LR image from the wind velocity and solar irradiance test datasets at different scaling factors (4×, 8×, 16×, 32×, and 64×). Figs. 3, 4, and 5 present semivariograms of the SR results (8×, 16×, and 32×) generated by different models for a randomly sampled LR image from the wind velocity and solar irradiance test datasets.

Corresponding author: Guofeng Cao.

Guiye Li and Guofeng Cao are with the Department of Geography, University of Colorado Boulder, Boulder, CO, 80309-0260, USA. (e-mail: Guiye.Li@colorado.edu; Guofeng.Cao@colorado.edu)

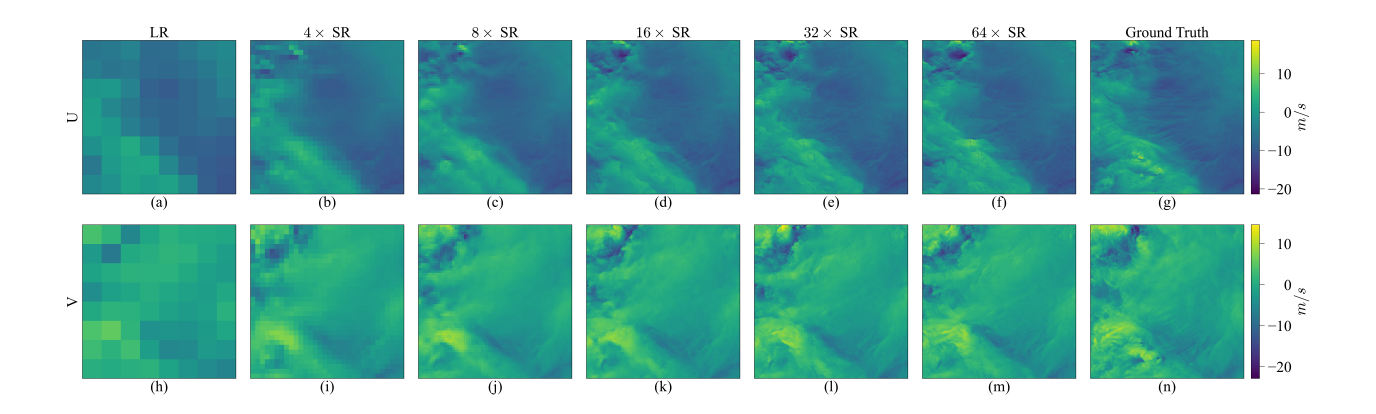


Fig. 1. SR results generated by the LAG-based downscaling framework for two channels (U and V) of a randomly sampled LR image from the wind velocity test dataset. The leftmost column [(a) and (h)] shows the input LR images at two channels (with image size 8×8), the rightmost column [(g) and (n)] shows the corresponding HR ground truth images (with image size 512×512). The columns in between shows the SR results at different scaling factors. [(b) and (i)]: $4 \times SR$ results with image size 32×32 ; [(c) and (j)]: $8 \times SR$ results with image size 64×64 ; [(d) and (k)]: $16 \times SR$ results with image size 128×128 ; [(e) and (l)]: $32 \times SR$ results with image size 256×256 ; [(f) and (m)]: $64 \times SR$ results with image size 512×512 .

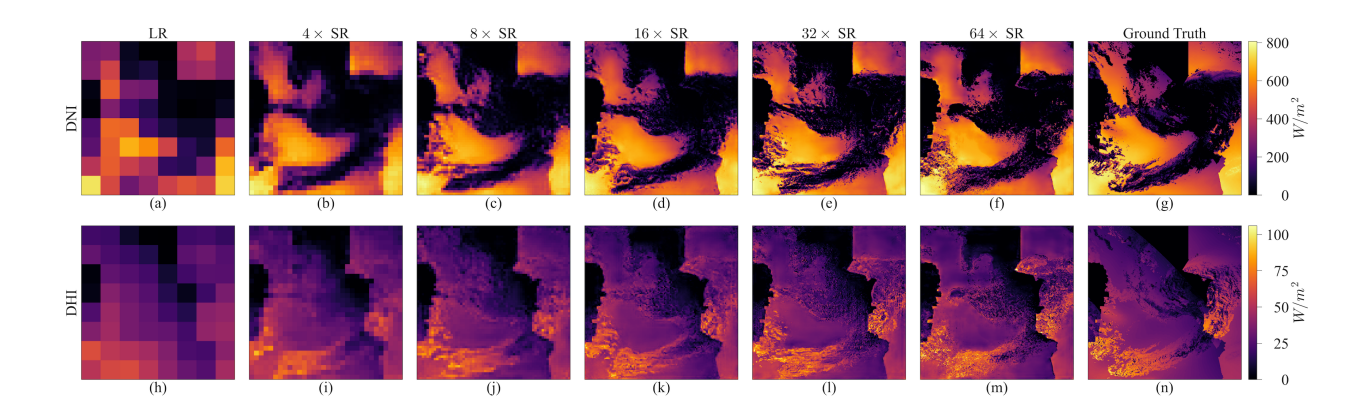


Fig. 2. SR results generated by the LAG-based downscaling framework for two channels (*DNI* and *DHI*) of a randomly sampled LR image from the solar irradiance test dataset. The leftmost column [(a) and (h)] shows the input LR images at two channels (with image size 8×8), the rightmost column [(g) and (n)] shows the corresponding HR ground truth images (image size 512×512). The columns in between shows the SR results at different scaling factors. [(b) and (i)]: 4×8 results with image size 32×32 ; [(c) and (j)]: 8×8 results with image size 64×64 ; [(d) and (k)]: 16×8 results with image size 128×128 ; [(e) and (l)]: 32×8 results with image size 256×256 ; [(f) and (m)]: 64×8 results with image size 512×512 .

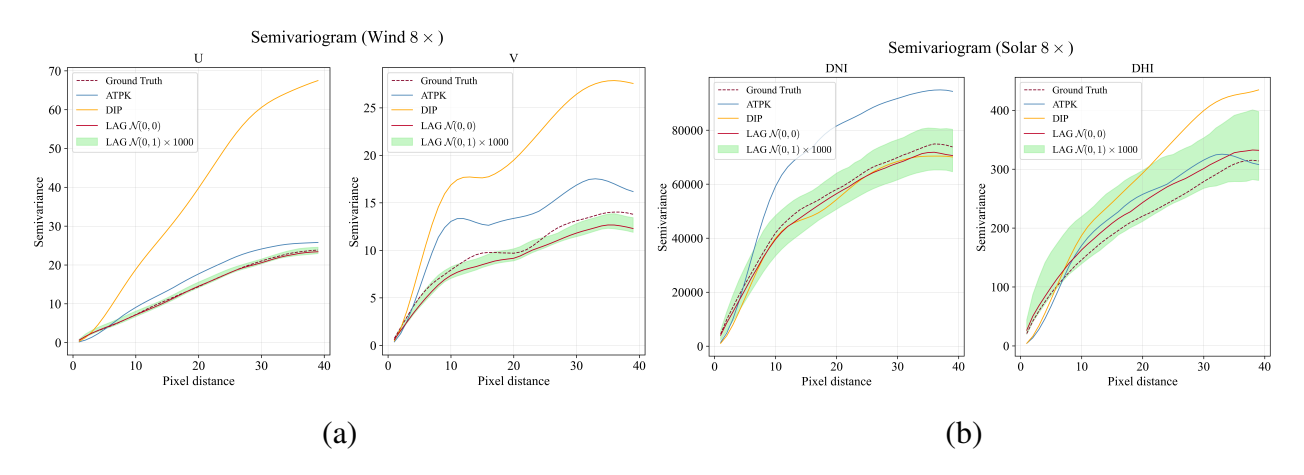


Fig. 3. Semivariograms of the $8 \times$ SR results generated by different models for a randomly sampled LR image from (a) wind velocity and (b) solar irradiance test datasets.

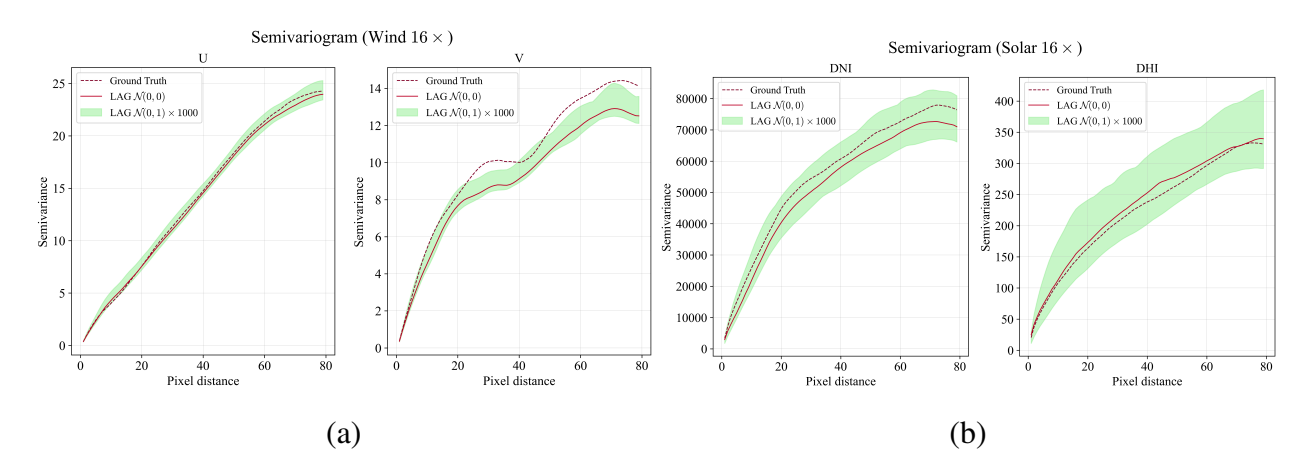


Fig. 4. Semivariograms of the $16 \times$ SR results generated by the LAG-based downscaling framework for a randomly sampled LR image from (a) wind velocity and (b) solar irradiance test datasets.

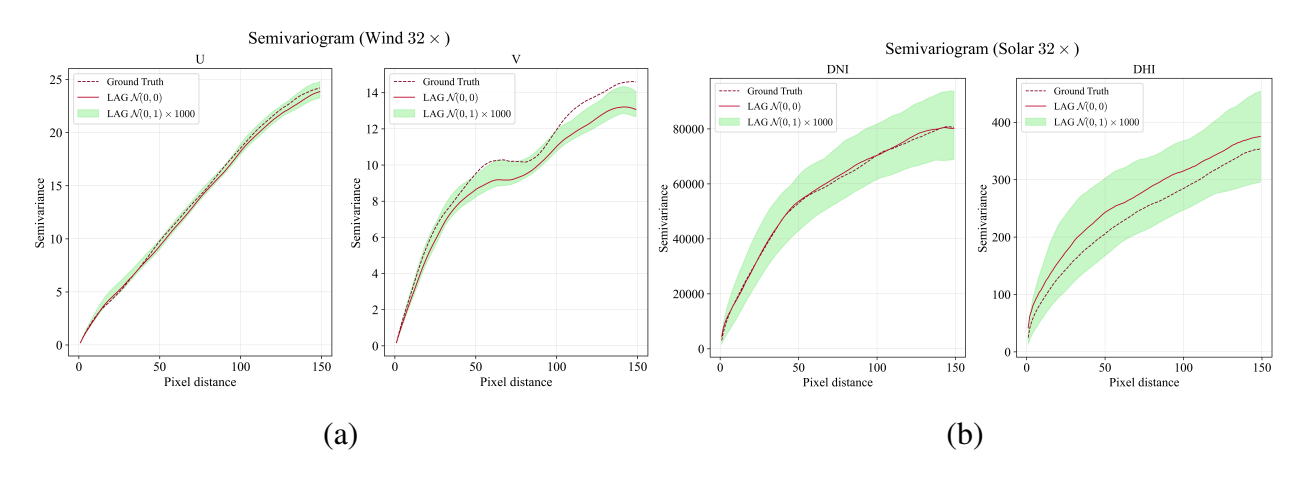


Fig. 5. Semivariograms of the $32 \times$ SR results generated by the LAG-based downscaling framework for a randomly sampled LR image from (a) wind velocity and (b) solar irradiance test datasets.